



Electrochemical Lithium Insertion into TiO₂ Anatase ALD Thin Films for Li-Ion Microbatteries: An Atomic-Scale Picture Provided by Raman Spectroscopy

Ankush Bhatia, Maxime Hallot, Clément Leviel, Pascal Roussel, Jean Pierre Pereira-Ramos, Christophe Lethien, Rita Baddour-Hadjean

► To cite this version:

Ankush Bhatia, Maxime Hallot, Clément Leviel, Pascal Roussel, Jean Pierre Pereira-Ramos, et al.. Electrochemical Lithium Insertion into TiO₂ Anatase ALD Thin Films for Li-Ion Microbatteries: An Atomic-Scale Picture Provided by Raman Spectroscopy. *Advanced Materials Interfaces*, 2023, 10 (10), pp.2202141. 10.1002/admi.202202141 . hal-04033995

HAL Id: hal-04033995

<https://hal.science/hal-04033995>

Submitted on 17 Mar 2023

HAL is a multi-disciplinary open access archive for the deposit and dissemination of scientific research documents, whether they are published or not. The documents may come from teaching and research institutions in France or abroad, or from public or private research centers.

L'archive ouverte pluridisciplinaire **HAL**, est destinée au dépôt et à la diffusion de documents scientifiques de niveau recherche, publiés ou non, émanant des établissements d'enseignement et de recherche français ou étrangers, des laboratoires publics ou privés.



Distributed under a Creative Commons Attribution 4.0 International License

Electrochemical Lithium Insertion into TiO_2 Anatase ALD Thin Films for Li-Ion Microbatteries: An Atomic-Scale Picture Provided by Raman Spectroscopy

Ankush Bhatia,* Maxime Hallot, Clément Leviel, Pascal Roussel, Jean-Pierre Pereira-Ramos, Christophe Lethien, and Rita Baddour-Hadjian*

Electrochemical lithium (de)intercalation in an atomic layer deposited (ALD) TiO_2 anatase thin film deposited on a planar Si / Al_2O_3 /Pt substrate is investigated by Raman spectroscopy. An initial discharge capacity of $63 \mu\text{Ah cm}^{-2} \mu\text{m}^{-1}$ ($0.5 \text{ Li}^+ \text{ mole}^{-1}$) is reached at C/10 rate, which increases up to $77 \mu\text{Ah cm}^{-2} \mu\text{m}^{-1}$ upon further cycles. An excellent capacity retention is achieved over at least 100 cycles, showing the good adherence of the ALD thin film. Raman spectra of Li_xTiO_2 ($0 \leq x \leq 0.5$) thin film electrodes point to the nucleation of the orthorhombic lithiated titanate (LT) $\text{Li}_{0.5}\text{TiO}_2$ phase from $x = 0.1$. This LT phase coexists with tetragonal TiO_2 in the $0.1 \leq x \leq 0.4$ composition domain to be pure for $x = 0.5$. A fully reversible transformation from orthorhombic LT to tetragonal TiO_2 is observed upon the charge. The high quality of the Raman spectra allows identifying for the first time 12 modes in the 100 – 800 cm^{-1} region for the electrochemically formed LT phase. Furthermore, an appropriate Raman spectra analysis allows a reliable and quantitative determination of the thin film composition during discharge and charge. These results illustrate Raman spectroscopy is a powerful probe to scrutinize the Li insertion/extraction mechanism in TiO_2 thin films.

1. Introduction

Thin film solid-state Li microbatteries are becoming the best choice for stand-alone sensor applications like radio-frequency identification tags, smart cards, wearable devices as well as

the Internet of things (IoT).^[1] Such applications have created a high demand for Li-ion microbatteries with high energy density. Up to now, the vast majority of commercial microbatteries use transition metal oxides active materials at the cathode side, e.g. LiCoO_2 ,^[2] V_2O_5 ,^[3] $\text{LiMn}_{1.5}\text{Ni}_{0.5}\text{O}_4$,^[4] or phosphate-based materials such as LiFePO_4 ,^[5] or LiMnPO_4 .^[6] At the anode side, Li-metal is commonly used due to its interesting characteristics such as low molecular weight which leads to a high specific capacity of 3828 mAh g^{-1} and high reducing character ($E_{\text{Li}^+/\text{Li}} = -3.05 \text{ V}$ vs standard hydrogen electrode (SHE)). However, the Li metal reactivity toward the air and the humidity imposes several constraints, especially battery encapsulation to protect the lithium against the environment. Furthermore, the low melting point of lithium (181°C) excludes or makes difficult specific assembling processes used

to integrate the components directly on the electronic circuit, for instance, the solder-reflow process involving a temperature peak at 260°C . Therefore, further development of thin film anode materials plays a crucial part in the development of Li-ion microbatteries.^[7]

A. Bhatia, J.-P. Pereira-Ramos, R. Baddour-Hadjian
 Institut de Chimie et des Matériaux Paris-Est (ICMPE)
 UMR 7182 CNRS-UPEC, 2 rue Henri Dunant, F-94320 Thiais, France
 E-mail: ankush_bhatia@yahoo.com; rita.baddour-hadjian@cnrs.fr
 M. Hallot, C. Leviel, C. Lethien
 Univ. Lille
 CNRS
 Univ. Polytechnique Hauts-de-France
 UMR 8520 – IEMN – Institut d'Electronique de Microélectronique et de Nanotechnologie
 F-59000 Lille, France

The ORCID identification number(s) for the author(s) of this article can be found under <https://doi.org/10.1002/admi.202202141>.
 © 2023 The Authors. Advanced Materials Interfaces published by Wiley-VCH GmbH. This is an open access article under the terms of the Creative Commons Attribution License, which permits use, distribution and reproduction in any medium, provided the original work is properly cited.

DOI: [10.1002/admi.202202141](https://doi.org/10.1002/admi.202202141)

M. Hallot, C. Leviel, C. Lethien
 Réseau sur le Stockage Electrochimique de l'Energie (RS2E)
 CNRS FR 3459, 33 rue Saint Leu, 80039 Amiens Cedex, France
 C. Leviel, P. Roussel
 Université de Lille
 Centrale Lille
 Université d'Artois
 Unité de Catalyse et de Chimie du Solide (UCCS)
 UMR 8181 CNRS, F-59000 Lille, France
 C. Lethien
 Institut Universitaire de France
 75005 Paris, France

In the last decade, several alternative materials have been proposed and thoroughly studied to overcome the limitations of Li-metal anodes: Li-metal alloys, silicon, germanium, and tin-based materials. However, despite providing greater capacities, the common problem of these materials is their huge volume expansion upon cycling.^[8] To overcome these drawbacks, low-voltage oxides have been extensively studied as negative electrode materials, especially titanium-based oxides such as TiO_2 and $\text{Li}_4\text{Ti}_5\text{O}_{12}$ that exhibit working potential lying within the thermodynamic stability window of conventional organic carbonate electrolytes (>0.8 V vs Li^+/Li), environmental friendliness, high safety, and low cost.^[9] Among the different TiO_2 polymorphs, tetragonal anatase exhibits the most attractive properties due to an easier lithiation/delithiation reaction, low volume change (<4%) during Li ion insertion/deinsertion process, short paths for fast lithium ion diffusion, flat discharge voltage plateau, and excellent cycling stability.^[9] Some inherent drawbacks of TiO_2 such as its relatively low theoretical capacity and electrical conductivity have motivated various strategies to solve these problems.^[10]

Interestingly, TiO_2 thin films have been the subject of numerous studies for applications in photo-electrochemical solar cells^[11] and Li-ion microbatteries.^[12–17] Haridas et al. reported the electrochemical performance of a 135 μm thick TiO_2 electrode deposited by spray pyrolysis technique that yielded to ultra-high areal capacity and volumetric capacities of 3.7 mAh cm^{-2} and 274 mAh cm^{-3} , respectively at 1C rate (1C = 335 $\mu\text{Ah mg}^{-1}$, for 21 mg cm^{-2} of mass loading) in 1 M LiPF_6 ethylene carbonate (EC):dimethyl carbonate (DMC) electrolyte.^[12] Lakshmi–Narayana et al. examined the electrochemical properties in 1 mol L^{-1} Li_2SO_4 aqueous solution of TiO_2 thin films deposited by electron-beam evaporation on multilayered Au/Ti/SiO₂/Si substrate.^[13] At a high current density of 1 mA cm^{-2} , a discharge capacity of 74 $\mu\text{Ah cm}^{-2} \mu\text{m}^{-1}$ (corresponding to 0.6 Li uptake) was obtained. Another work by Curcio et al.^[14] on pulsed laser deposited anatase-based TiO_2 nanoparticles on aluminum substrate reported a capacity of \approx 11 $\mu\text{Ah cm}^{-2}$ at 1 $\mu\text{A cm}^{-2}$, using LiPF₆ EC: DMC electrolyte. Interestingly, using atomic layer deposition (ALD), Eustache et al. successfully performed conformal deposition of anatase TiO_2 layer (38 to 150 nm thick) on a 3D surface structure.^[15,16] Electrochemical measurements in standard liquid electrolytes allow achieving surface discharge capacities of 200 $\mu\text{Ah cm}^{-2}$ at C/10 for the 150 nm thin film, the highest one reported for a TiO_2 negative electrode deposited on a 3D topology.

Many papers have reported the phase transformation behavior upon Li electrochemical insertion into TiO_2 anatase. From early ex situ X-ray diffraction (XRD) study in 1985, Li insertion in bulk anatase TiO_2 was found to produce an orthorhombic lithium titanate (LT) $\text{Li}_{x=0.5}\text{TiO}_2$ phase through a diphasic transition occurring at 1.78 V versus Li^+/Li , leading to a specific capacity of 168 mAh g^{-1} .^[18] Later, many other works based on NMR,^[19,20] neutron diffraction,^[21,22] and Raman spectroscopy,^[23–26] confirmed this spontaneous phase separation into Li-poor ($\text{Li} \approx 0.01$) and Li-rich ($\text{Li} \approx 0.5$) domains. However, when TiO_2 is synthesized at the nanometric scale, several studies have described a progressive Li-ion solubility increase as well as an extension of the solid solution domain as the particle size is reduced,^[25,27–31] with electrochemical performance

strongly depending on the particle size.^[25,30–34] In spite of such nano-size effects, the Li insertion/extraction mechanism into TiO_2 anatase thin film has been scarcely reported. This is probably due to the difficulty to carry out conventional XRD experiments on thin films, owing to the small diffraction volume as well as ill-defined and broad diffraction peaks usually exhibited by small crystallite-size materials.^[35]

Raman spectroscopy on the other hand is capable of probing short-range structures^[36–39] and was proved to be efficient to discriminate the orthorhombic and tetragonal phases in the Li/TiO_2 system.^[23–26] However, this technique has been mainly carried out for the characterization of the lithium insertion/extraction mechanism in bulk TiO_2 .^[23–26] In 2004, Baddour-Hadjean et al. reported the first ex situ Raman spectra of Li_xTiO_2 composite electrodes during the discharge-charge cycle of anatase.^[23,24] The Raman fingerprint obtained for the fully lithiated $\text{Li}_{0.5}\text{TiO}_2$ composite electrode, made of 12 modes, was fully assigned thanks to the help of lattice dynamics simulations. In 2007, Hardwick et al. performed in situ Raman spectroscopy experiments on various nano-scale TiO_2 anatase powders and showed a noticeable effect of the crystallite size on the electrochemical reaction as well as the width of the solid solution domain.^[25] In 2013, with the help of isotope labeling, Kavan et al. reported the Raman spectra of electrochemically and chemically lithiated TiO_2 anatase powders, with a slightly better spectral resolution of the latter that allow the authors to identify 20 modes in the experimental Raman spectrum of LT.^[26] These works reported in unison that Li-insertion in the anatase TiO_2 powder caused the disappearance of the six anatase Raman lines ($I_{41}/\text{amd-D}^{19}4_{\text{h}}$), to the benefit of novel features attributed to the orthorhombic LT phase ($Imma\text{-D}^{28}2_{\text{h}}$). Regarding TiO_2 thin films, one single paper from Dinh et al. in 2003 showed a significant perturbation of the anatase Raman spectrum upon electrochemical lithiation of sol-gel TiO_2/ITO electrochromic thin films, with the appearance of 5 broad and ill-defined bands that the authors tentatively attributed to the LT phase.^[40]

This paper intends to add the lacking knowledge in the field of thin films materials by exploring the electrochemical Li insertion mechanism in ALD-deposited TiO_2 anatase thin films, using Raman spectroscopy. The electrochemical properties of the TiO_2 thin film are examined in 1 M LiClO_4 EC: DMC 1:1 liquid electrolyte. Then, ex situ Raman spectra are collected during the first discharge-charge cycle and accurately analyzed to picture the structural changes accompanying lithium insertion/extraction in Li_xTiO_2 thin film electrodes ($0 \leq x \leq 0.5$).

2. Results and Discussion

2.1. Characterization of the TiO_2 Thin Film

Figure 1a shows the schematic of the stacked layers on the Si wafer. Typically, this stacking is composed of several layers (from bottom to top Si (0.385 mm)/ Al_2O_3 (100 nm)/Pt current collector (50 nm)/ TiO_2 (150 nm)/ Li_3PO_4 (3 nm)). The cross-sectional scanning electron microscopy (SEM) image shown in Figure 1b reveals that all the layers of the functional Si/ Al_2O_3 / Pt/ TiO_2 stacking are well segregated and exhibit

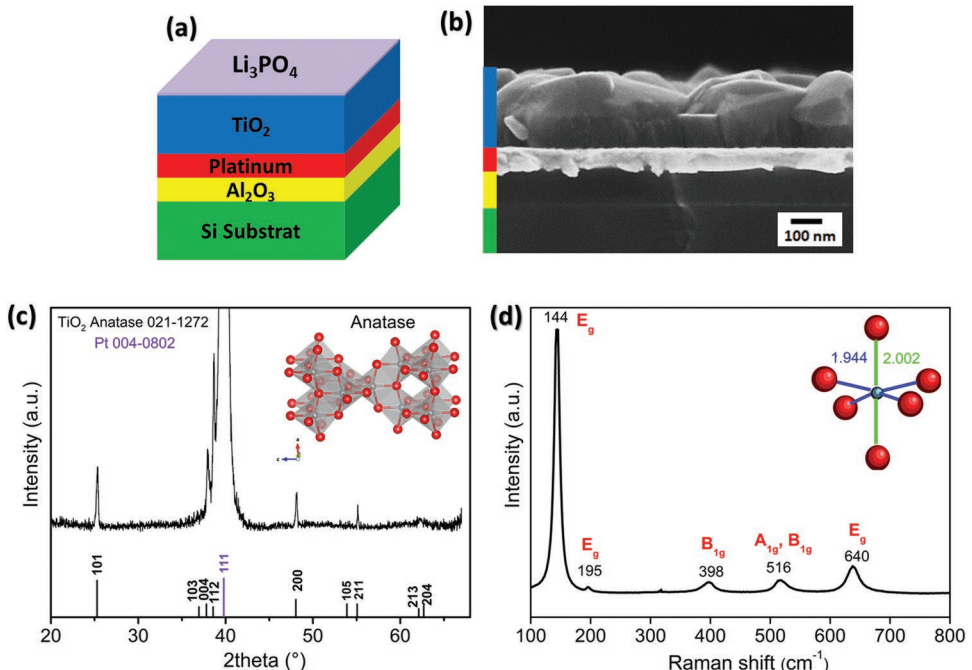


Figure 1. a) Schematic of the Si/Al₂O₃/Pt/TiO₂/LPO layers stacking, b) SEM cross-section analysis of the Si/Al₂O₃/Pt/TiO₂ stacking, c) XRD pattern of the TiO₂ thin film, in insert: structure of anatase TiO₂, d) Raman spectrum of the TiO₂ thin film, in insert: octahedral Ti environment.

uniform thickness with flat and sharp interfaces at the nanoscale level and no interdiffusion between the layers, as expected from thin films deposited by ALD technique.^[41,42] Hallot et al.^[43] have well explained the purpose of introducing a dense Al₂O₃ layer in the stacking, capable of preventing the Pt–Si interdiffusion leading to the formation of PtSi alloy. Moreover, the 3 nm thick Li₃PO₄ solid-electrolyte layer deposited on the top of the TiO₂ layer acts as a good ionic conductor and electronic insulator, and has been reported as a good protective layer.^[15,43] The XRD pattern of the TiO₂ thin film is shown in Figure 1c. Note that peaks observed at 36° and 40° correspond to the (111) diffraction plane of the platinum current collector (JCPDS PDF 00-004-0802), the first one is due to the K-β X-ray emission line that is not completely filtered in this high-flux configuration. All the other diffraction peaks correspond to a pure anatase structure (JCPDS number 021-1272) and are indexed using a body-centered tetragonal symmetry (space group I4₁/amd-D¹⁹_{4h}). The refined cell parameters of $a = b = 3.7838(4)$ Å and $c = 9.495(3)$ Å are in good agreement with the powder diffraction data. Broadening of the Bragg peaks is typical of the presence of a nano-sized material. An average apparent crystallite size of 50 nm is found, using a fundamental parameters approach implemented in the JANA2006 software.^[44] The crystal structure of TiO₂ anatase (insert of Figure 1c) is made of zig-zag chains located in close-packed planes, titanium ions occupying half of the 4a octahedral sites and oxygen atoms sitting in the 8e tetrahedral sites. Each [TiO₆] octahedron shares two adjacent edges with other [TiO₆] units in the (b, c) plane to form infinite, planar double chains parallel to *a* and *b* directions. These double chains share corners with identical chains above and below and are shifted along the *c*-axis with respect to each other. Finally, all [TiO₆] octahedra share four edges and all oxygen ions are

bonded to three titanium ions. The empty octahedral sites also comprise double chains that may be similarly described.

Raman spectroscopy is an appropriate structural method to differentiate between the different polymorphs of TiO₂.^[45–53] There has already been several papers devoted to the lattice dynamics study of anatase TiO₂.^[23,24,52] According to factor group analysis, the 15 optical modes of anatase TiO₂ have the following irreducible representation:

$$\Gamma_{\text{opt}}(\text{TiO}_2) = 1A_{1g} + 1A_{2u} + 2B_{1g} + 1B_{2u} + 3E_g + 2E_u \quad (1)$$

The A_{1g} , B_{1g} , and E_g modes are Raman active and thus, six fundamental transitions are expected in the Raman spectrum of anatase TiO₂:

$$\Gamma_{\text{Raman}}(\text{TiO}_2) = 1A_{1g} + 2B_{1g} + 3E_g \quad (2)$$

The experimental Raman spectrum of the TiO₂ thin film (Figure 1d) displays the typical fingerprint of anatase at room temperature, showing five main bands located at 144 cm⁻¹ (E_g mode), 195 cm⁻¹ (E_g mode), 398 cm⁻¹ (B_{1g} mode), 516 cm⁻¹ (merged A_{1g} and B_{1g} modes), and 640 cm⁻¹ (E_g mode) corresponding to O–Ti–O bending and Ti–O stretching modes.

2.2. Electrochemical and Structural Study

2.2.1. Electrochemical Study

The typical discharge–charge curves for the TiO₂ thin film are shown in Figure 2a.

Starting from the open circuit voltage (OCV) of 2.8 V, after an abrupt fall down to ca. 1.95 V, the voltage decreases

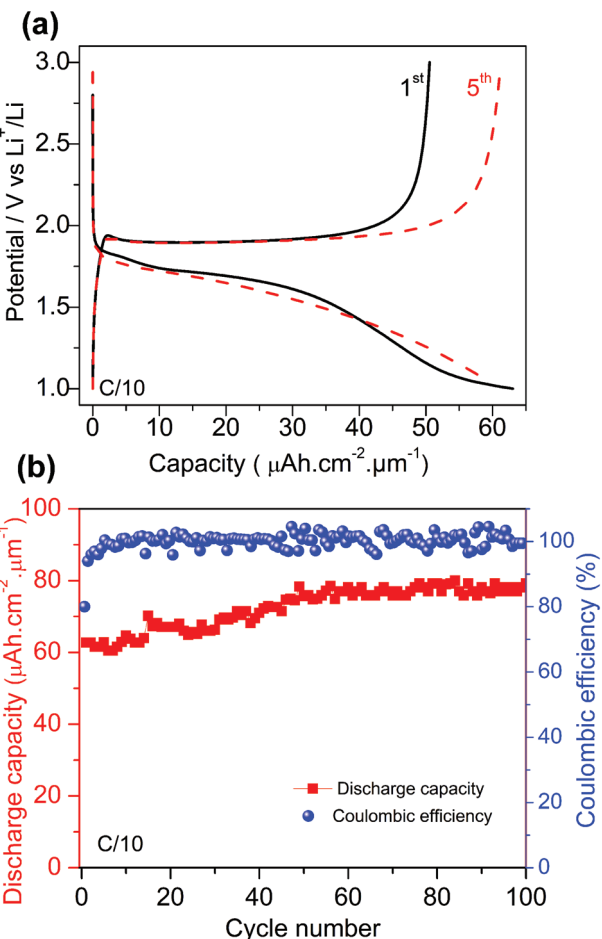


Figure 2. Electrochemical properties of the TiO_2 thin film. a) First and fifth discharge-charge cycle in black solid line and red dashed line, respectively; b) Evolution of the discharge capacity and coulombic efficiency versus number of cycles. 1 M LiClO_4 / EC:DMC (1:1 vol.%) electrolyte. 3–1 V voltage window. C/10 rate ($0.75 \mu\text{A cm}^{-2}$).

monotonically to 1.75 V, then a quasi-voltage plateau is observed in the 1.7 V region followed by a sloping curve down to 1 V. The first discharge capacity is $63 \mu\text{Ah cm}^{-2} \mu\text{m}^{-1}$ (which corresponds to 0.5 Li uptake/mole of oxide) assuming a density of 3.75 g cm^{-3} for our TiO_2 thin films.^[41,44]

The charge process exhibits a flat potential plateau at 1.9 V and involves a slightly lower capacity value of $50 \mu\text{Ah cm}^{-2} \mu\text{m}^{-1}$, as usually observed for micrometric anatase TiO_2 .^[23,33] However, from the fifth cycle, the same capacity value of $61 \mu\text{Ah cm}^{-2} \mu\text{m}^{-1}$ is reached on discharge and charge, indicating a fully reversible Li insertion-extraction process.

Cycling experiments at C/10 reveal an overall capacity increase during the 50 cycles, from 63 to $77 \mu\text{Ah cm}^{-2} \mu\text{m}^{-1}$ (corresponding to 0.61 Li/mole of oxide), which then stabilizes over at least 50 cycles (Figure 2b). This capacity increase was also reported for 60 nm thick ALD thin films and explained by an electrochemical activation of crystallites in the layer.^[15] The excellent capacity retention achieved over at least 100 cycles, is related to the minor volume expansion experienced by TiO_2 anatase upon lithium insertion (i.e., 2.4%), but also demonstrates the good adherence of the present ALD TiO_2 thin films.

2.2.2. Study of the Li Insertion/Extraction Mechanism During the First Discharge-Charge Cycle

The structural changes induced in the TiO_2 thin film by the electrochemical Li insertion/extraction have been explored using Raman spectroscopy. Previous studies on bulk TiO_2 describe a tetragonal TiO_2 ($I4_1/\text{amd}$ - D_{4h}^{19}) to orthorhombic Li_xTiO_2 ($Imma$ – D_{2h}^{28}) transformation upon lithium insertion.^[18–26] In the LT structure, Li^+ ions occupy multiple positions inside the oxygen octahedra.^[22] The equivalent amount of Ti^{4+} is reduced to Ti^{3+} as Li^+ ions are inserted into the structure, and first principle calculations have reported that the structural stability of the electroformed $\text{Li}_{0.5}\text{TiO}_2$ is associated with the similarity of the ionic radii of Li^+ and Ti^{3+} ions (0.74 and 0.67 Å, respectively).^[53]

The tetragonal-to-orthorhombic distortion implies a symmetry reduction from D_{4h} to D_{2h} . Therefore, A_{1g} and $2B_{1g}$ modes of the anatase lattice transform into $3A_g$ modes of the LT lattice, and the $3E_g$ modes of the anatase lattice split into $3B_{2g}$ and $3B_{3g}$ modes of the LT lattice.^[23,24] In addition, three Li modes involving displacements of the Li atoms along x (B_{2g}), y (B_{3g}), and z (A_g) directions appear. In total, the Raman spectrum of the LT phase consists of 12 modes distributed as:

$$\Gamma_{\text{Raman}}(\text{LT}) = 4A_g + 4B_{2g} + 4B_{3g} \quad (3)$$

The Raman spectra of the Li_xTiO_2 electrodes recorded at different x values ($0 \leq x \leq 0.5$) during the first discharge at C/10 rate are shown in Figure 3. The discharge curve shown in Figure 3a marked with different color sphere symbols shows the different investigated x values in Li_xTiO_2 . Note that whatever the x value, similar spectra were found for the 10 investigated areas, showing the good homogeneity of the lithiation.

A thorough examination of the Raman spectra collected during the discharge (Figure 3b,c) leads to the following comments:

- i) The Raman spectra of the initial anatase TiO_2 electrode, with Raman bands at 144 , 195 , 398 , 516 , and 640 cm^{-1} is not altered up to $x=0.05$, indicating the 0.05 composition is the limit of the solid solution domain.
- ii) From $x=0.1$, the spectral profile is greatly changed with several new components appearing in the 100 – 800 cm^{-1} wavenumber range, pointing to the beginning of the tetragonal to the orthorhombic phase transition. In the low-frequency region, the intense E_g mode at 144 cm^{-1} is replaced by three bands located at 152 , 168 , and 183 cm^{-1} while new peaks appear at 225 , 236 , 318 , and 348 cm^{-1} . In the middle-frequency range, the band at 398 cm^{-1} is shifted to 416 cm^{-1} and two new components start to rise at 440 and 466 cm^{-1} . In the high-frequency range, the band at 520 cm^{-1} is replaced by two bands at 532 and 556 cm^{-1} while the 640 cm^{-1} peak shifts to 632 cm^{-1} .
- iii) On further Li insertion ($0.1 \leq x \leq 0.35$), the new bands at 168 and 182 cm^{-1} grow at the expense of the 152 cm^{-1} one.
- iv) At the end of the discharge ($0.4 \leq x \leq 0.5$), the Raman spectrum exhibits the full fingerprint of the LT $\text{Li}_{0.5}\text{TiO}_2$ phase, with 12 bands at 168 , 182 , 225 , 236 , 318 , 348 , 416 , 440 , 466 , 536 , 556 , and 632 cm^{-1} . Modes at 440 , 466 , and 556 cm^{-1} are related to Li-O vibrations while the others correspond to lattice modes perturbed by Li interactions (Figure 4).^[30,31]

This Raman study allows proposing of a phase diagram in the Li/TiO_2 thin film system. The $0 \leq x \leq 0.05$ composition range corresponds to a solid solution of tetragonal anatase

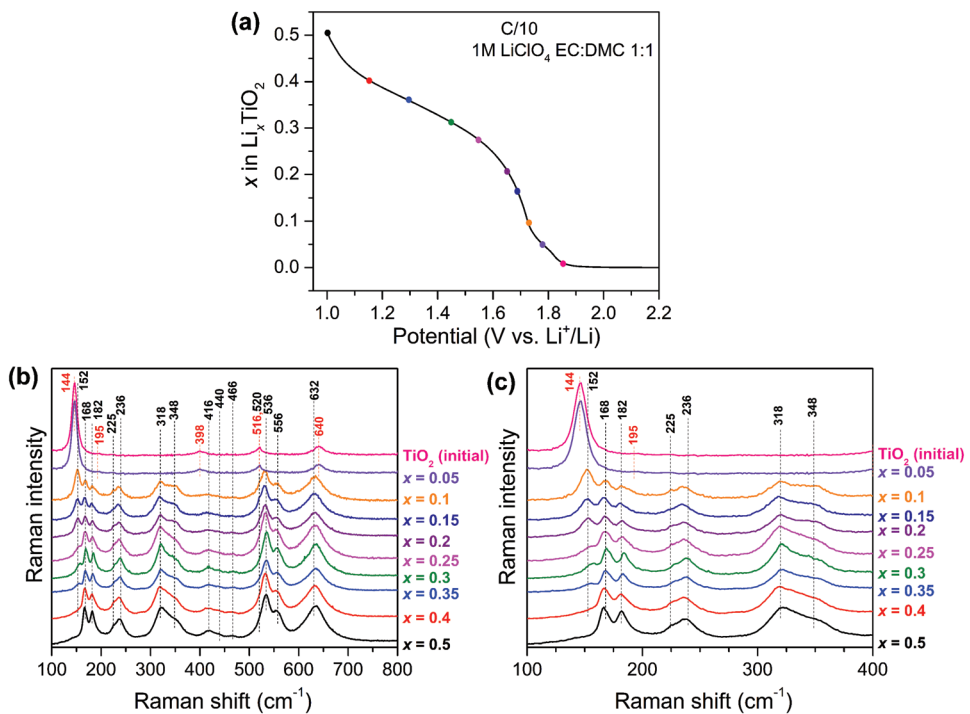


Figure 3. a) Evolution of the potential from OCV to 1 V versus x content in Li_xTiO_2 at C/10 rate, b) Continuum of Raman spectra recorded during the first discharge for electrochemically lithiated Li_xTiO_2 thin film electrodes ($0 \leq x \leq 0.5$), c) Enlarged view of the Raman spectra in the $100\text{--}400\text{ cm}^{-1}$ range.

Li_xTiO_2 (phase 1). In the $0.1 \leq x < 0.5$ composition range, a biphasic region of phase 1 and orthorhombic LT Li_xTiO_2 (phase 2) is observed, the phase 2 proportion increasing at the expense of phase 1 to be 100% for $x = 0.5$. The important spectral variations in the low wavenumber region ($100\text{--}200\text{ cm}^{-1}$) provide relevant descriptors of the tetragonal to orthorhombic transition. Indeed, an estimation of the proportion of the LT phase in the thin film electrode can be proposed by considering the relative area of the $168/182$ bands belonging to the LT phase to that of the $144/152$ bands assigned to TiO_2 . Selected Raman spectra fittings shown in **Figure 5** lead to the LT phase relative amounts at different states of discharge gathered in **Table 1**.

Figure 6 compares the estimation of the electrode compositions from the Raman spectroscopy analysis (represented by

black circles) to those issued from the faradaic yield involved during the electrochemical preparation (represented by a red line). It is noteworthy the remarkable agreement of x values in Li_xTiO_2 estimated by Raman with that obtained from the faradaic yield. This result demonstrates the reliability of our Raman analysis and its efficiency to provide an accurate estimation of the thin film electrode composition.

Figure 7 shows that reverse spectral changes occur during the charge. Indeed, the band at 152 cm^{-1} reappears as lithium is extracted, as shown for the electrode composition $\text{Li}_{0.26}\text{TiO}_2$ (in green) and the intensity of this band increases with further removal of Li from Li_xTiO_2 followed by the growth and reverse shift to 144 cm^{-1} . Above 1.9 V , this band increases at the expense of the orthorhombic B_{2g}/B_{3g} doublet at $168/182\text{ cm}^{-1}$. A complete restoration of the Raman spectrum of the tetragonal TiO_2 framework is observed at 3 V , with the main bands observed at $144, 195, 398, 516$, and 640 cm^{-1} .

The structural reversibility upon the cycling experiment examined by Raman spectroscopy is shown in **Figure 8**. The fingerprints of the thin film electrodes after one cycle and after 130 cycles clearly exhibit the typical Raman spectrum of the pristine TiO_2 electrode, indicating the excellent reversibility of the lithium insertion-extraction process and the good structural stability of the TiO_2 thin film at the scale of the chemical bond.

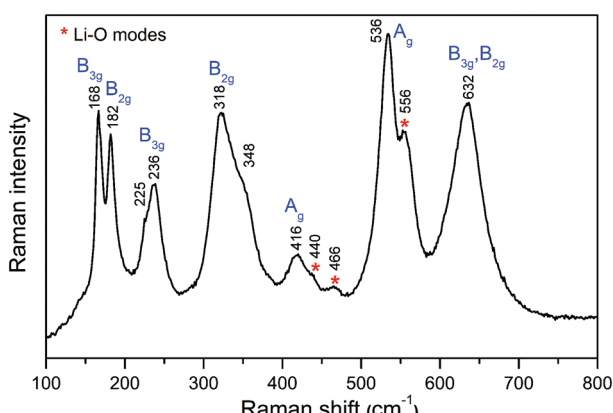


Figure 4. Raman spectrum of orthorhombic LT $\text{Li}_{0.5}\text{TiO}_2$ with its assignment.

3. Conclusion

In this work, Raman spectroscopy is carried out to explore the short-range environment on Li_xTiO_2 thin film electrode ($0 \leq x \leq 0.5$) with the pure anatase TiO_2 nanometric thin film being deposited by ALD on a platinum current collector. The

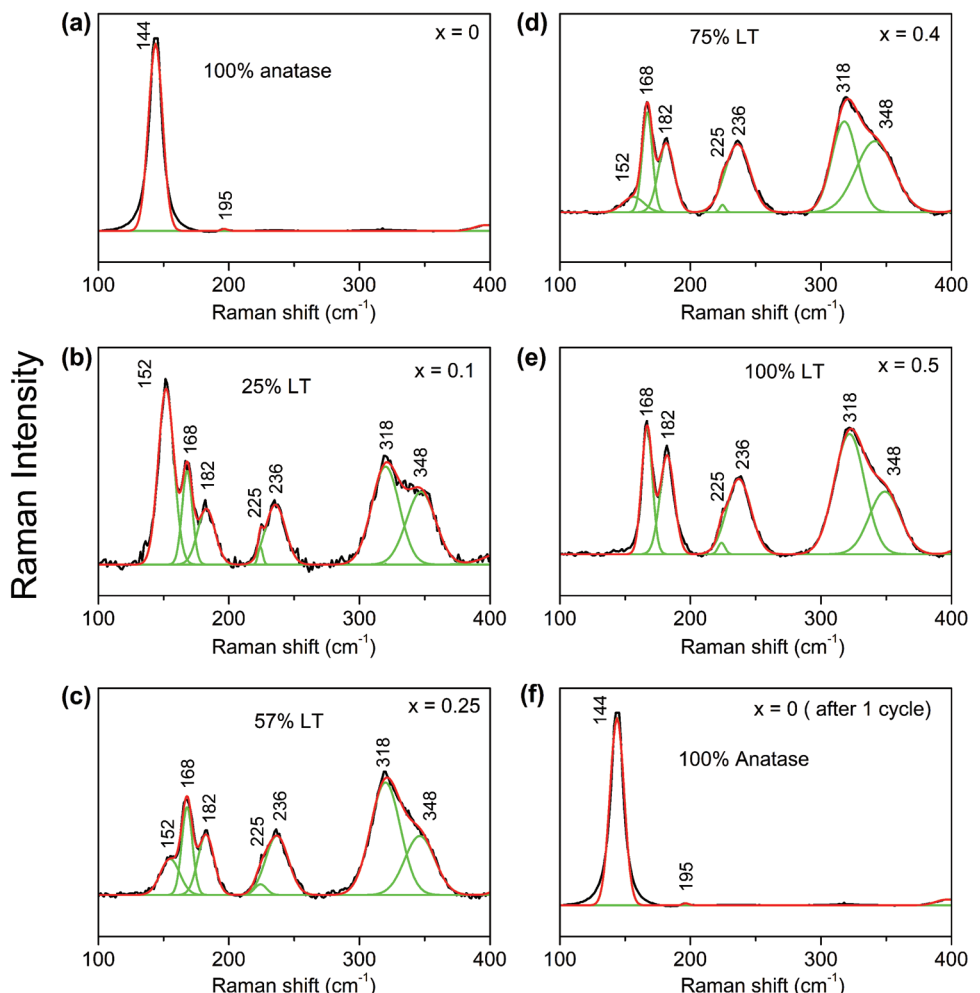


Figure 5. Raman spectra fittings in the 100–400 cm⁻¹ region of the Li_xTiO_2 anatase thin film at different depths of discharge during the first discharge ($0 \leq x \leq 0.5$) and after a discharge-charge cycle. LT : lithiated titanate phase.

Table 1. Proportion (in %) of LT phase in discharged Li_xTiO_2 thin film electrodes ($0 \leq x \leq 0.5$) obtained from the analysis of the Raman spectra, compared to that expected from the faradaic yield. Band A belongs to anatase (E_g mode at 144 cm⁻¹ and shifting to 152 cm⁻¹). Bands B and C belong to LT phase (168 and 182 cm⁻¹, respectively).

x in Li_xTiO_2 faradaic yield	% LT from faradaic yield	% LT from Raman B/(A + B)	% LT from Raman C/(A + C)	x in Li_xTiO_2 from Raman
0	0	0	0	0
0.1	20	25	26	0.125
0.15	30	33	34	0.165
0.2	40	39	39	0.195
0.25	50	57	58	0.287 ± 0.005
0.3	60	65	60	0.312 ± 0.012
0.35	70	72	70	0.355 ± 0.005
0.4	80	75	75	0.380 ± 0.050
0.5	100	100	100	0.5

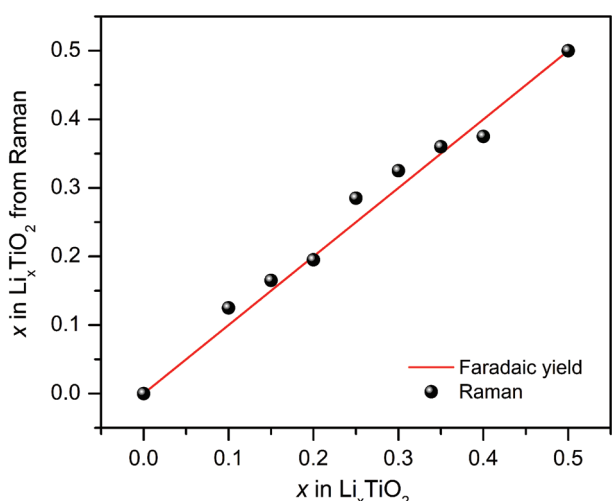


Figure 6. Estimation of x value in Li_xTiO_2 electrodes from Raman spectra analysis (black circles) compared to the faradaic yields involved during electrodes preparation (red line).

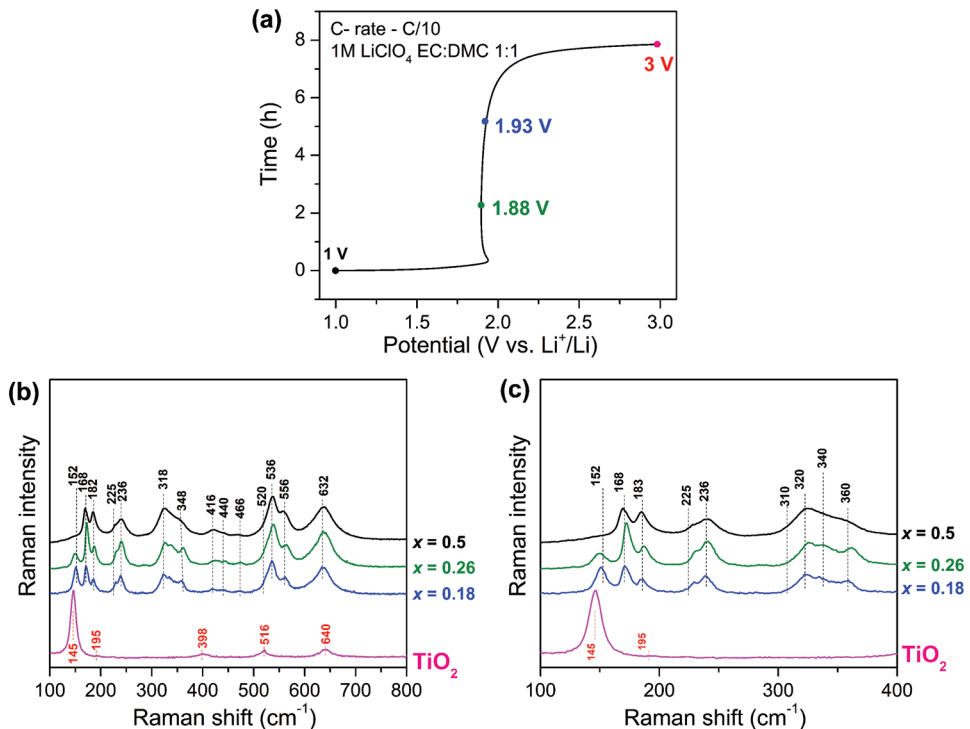


Figure 7. a) Evolution of the potential versus time during the charge at C/10 rate, b) Continuum of Raman spectra recorded during the charge for electrochemically delithiated Li_xTiO_2 thin film electrodes ($0 \leq x \leq 0.5$), c) Enlarged view of the Raman spectra in the 100–400 cm^{-1} range.

excellent adherence of the 150 nm thick deposit allows to reach a high reversible capacity value of $56 \mu\text{Ah cm}^{-2} \mu\text{m}^{-1}$ at C/10 in the 1 V–3 V voltage range and a remarkable stability of capacity over at least 100 cycles.

For the first time, detailed Raman spectra are obtained on TiO_2 thin films in a Li cell, providing a comprehensive picture of the structural changes induced by lithium intercalation during the first discharge-charge cycle. This study shows the electrochemical lithium reaction in the thin film is homogeneous and involves a 2-phases mechanism. From $x = 0.1$ Li^+ in Li_xTiO_2 , new Raman lines in the lower wavenumber point to the emergence of lithiated titanate with orthorhombic

structure ($\text{Imma}-\text{D}^{28}_{2h}$), that coexists with anatase in the $0.1 \leq x \leq 0.4$ composition range and is found to be single for $x = 0.5$. More interestingly, by considering the relative areas of appropriate Raman descriptors, an estimation of the proportion of each phase can be provided at each stage of the lithiation process. The relevance of our approach is confirmed by the remarkable agreement between the lithium uptake values calculated from the Raman analysis and the faradaic yields involved during the electrode preparation. In addition, a high structural reversibility after 100 cycles is revealed by Raman spectroscopy. While XRD is limited both by the small volume of active material in thin film configuration and the difficulty to discriminate between the fingerprint of the pristine and lithiated materials, this study clearly demonstrates the efficiency of Raman spectroscopy to provide at the laboratory scale a comprehensive and quantitative picture of the electrochemical lithiation mechanism in nanometric TiO_2 thin films.

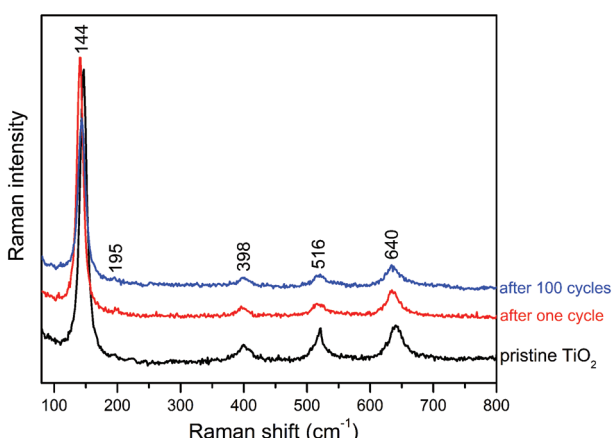


Figure 8. Raman spectra recorded on the initial TiO_2 thin film electrode, after the first charge and after 100 cycles at C/10. 1–3 V potential range.

4. Experimental Section

TiO₂ Thin Film Preparation: First, an aluminum oxide (Al_2O_3) layer (100 nm-thick) was deposited on a 3" silicon wafer by ALD in a PicoSun reactor. This layer acts as a diffusion barrier to prevent the interdiffusion between Pt and Si species leading to the formation of Pt-Si when deposition and/or post-annealing process is achieved.^[15] A Plassys MEB 550S equipment was used to evaporate a 50 nm-thick Platinum layer on the aluminum oxide layer. Then, the TiO_2 thin film was also deposited by ALD from a TFS200 Beneq ALD reactor, as already reported.^[15,16] The TiO_2 deposition was achieved using TiCl_4 (claimed purity 99.9999%, From Strem Chemical) as a metallic precursor and deionized water as an oxidant. The ALD reaction followed 4 steps using first TiCl_4 and then the water. Nitrogen was used as the purge and the carrier gas. The chamber

temperature was held at 250 °C in order to promote the formation of the desired anatase TiO₂ polymorph. The bottle temperature of the two precursors was kept at ≈20 °C as they operate at high vapor pressure. The thickness of the TiO₂ layer was measured at close to 150 nm. To stabilize the solid/liquid interface, a 3 nm-thick Li₃PO₄ (LPO) layer was deposited on the top of TiO₂ by ALD in a R200 PicoSun reactor at ≈2 mbar at 300 °C, using trimethylphosphate and lithium tert-butoxide from StremChemical (claimed purities of 97% and 98%, respectively).^[43] The electrochemical and structural study were carried out on the resulting Si/Al₂O₃/Pt/TiO₂/LPO stacked layers.

Morphological Analysis and Structural Characterization: The thickness and microstructure of the films were determined using a scanning electron microscope (Zeiss supra55-VP). The structure of the deposited TiO₂ thin film was determined with a Rigaku SMARTLAB multipurpose six-axis diffractometer (9 kW rotating anode) equipped with Cu-K α radiation ($\lambda = 1.5418 \text{ \AA}$). Cell parameters were refined using the JANA2006 software.^[44] Raman spectra were recorded with a LaBRAM HR 800 (Jobin-Yvon Horiba) Raman micro-spectrometer including Edge filters and equipped for signal detection with a back-illuminated charge-coupled device detector (Spex CCD) cooled by Peltier effect to 200 K. A He:Ne laser (632.8 nm) was used as the excitation source. The spectra were measured in back-scattering geometry. The spectral resolution was ≈0.5 cm⁻¹. A 100X objective was used to focus the laser light on the sample surface to a spot size of 1 μm². The power of the laser beam was adjusted to 0.2–0.5 mW with neutral filters of various optical densities in order to prevent any laser-induced damage of the sample. Raman spectra were systematically recorded on ten different spots of each sample, which gave similar fingerprints, showing the good homogeneity of the electrochemical reaction in the thin films.

Electrochemical Study: Electrochemical measurements were carried out in a homemade Teflon flat cell operated in an Ar-filled glove box (O₂ and H₂O quantities: less than 1 ppm). The cell is composed of two pieces of Teflon where the samples are sandwiched between the pieces. A hole of 0.442 cm² was drilled in the top piece, allowing the filling of the flat cell with the liquid electrolyte (2 mL of 1 M LiClO₄ anhydrous, 99% dissolved in ethyl carbonate EC (C₃H₆O₃, anhydrous, 99%) and dimethyl carbonate DMC (C₃H₆O₃, anhydrous, 99%) (EC:DMC, 1:1). An O-ring was used to seal the sample/top piece interface and to define an analyzed electrode surface area of 0.442 cm². The cell was assembled with TiO₂ thin film as a working electrode and pure lithium metal foil, which acts as both a reference and counter electrode. The two electrodes were separated by a Whatmann glass fiber soaked in the electrolyte. The 1 M LiClO₄ EC: DMC 1:1 electrolyte was prepared in an argon-filled glovebox (0.1 ppm of O₂/0.1 ppm of H₂O). The water content of the electrolyte solution was analyzed by Karl Fischer titration and was found to be below 20 ppm. The measurements were performed at 20°C using a multichannel BioLogic VMP3 potentiostat. The Raman investigation was carried out in the 1–3 V versus Li⁺/Li potential window in the two electrodes flat-cell, during the first charge–discharge cycle of TiO₂. The cells were discharged (and charged) at C/10 rate (0.75 μA cm⁻²) up to the required x composition in Li_xTiO₂ (0 ≤ x ≤ 0.5). The current supply was stopped when the desired x content was reached and the cells were disassembled in the glove box. The thin film electrodes were rinsed three times with DMC in order to remove any electrolyte residue and placed in an airtight Raman cell to be analyzed by Raman spectroscopy.

Acknowledgements

This research was financially supported by the ANR within the CASSIOPEES project (ANR-17-CE09-0016-01). The authors also wish to thank the French network on electrochemical energy storage (RS2E) and the Store-Ex Labex for their support. The French RENATECH network is greatly acknowledged for the use of microfabrication facilities. Chevreul Institute (FR CNRS 2638) is acknowledged for funding.

Conflict of Interest

The authors declare no conflict of interest.

Author Contributions

M.H., C.L., P.R., and Ch.L. were involved in the thin film deposition and XRD characterization. A.B., J.P.P.R., and R.B.H. were involved in electrochemical and Raman analyses. Ch.L., J.P.P.R., and R.B.H. planned the project. R.B.H., A.B., and J.P.P.R. wrote the paper. All the authors discuss about the obtained results and approve the manuscript before submission.

Data Availability Statement

The data that support the findings of this study are available from the corresponding author upon reasonable request.

Keywords

anode materials, atomic layer deposition, Li-ion micro-batteries, lithiated titanate Li_{0.5}TiO₂, Raman spectroscopy, thin film, TiO₂ anatase

Received: September 29, 2022

Revised: January 4, 2023

Published online:

- [1] J. F. M. Oudenhoven, L. Baggetto, P. H. L. Notten, *Adv. Energy Mater.* **2011**, *1*, 10.
- [2] S. Tintignac, R. Baddour-Hadjean, J. P. Pereira-Ramos, R. Salot, *Electrochim. Acta* **2012**, *60*, 121.
- [3] C. Navone, R. Baddour-Hadjean, J. P. Pereira-Ramos, R. Salot, *J. Electrochem. Soc.* **2009**, *156*, A763.
- [4] M. Hallot, P. Roussel, C. Lethien, *ACS Appl. Energy Mater.* **2021**, *4*, 3101.
- [5] X.-J. Zhu, L.-B. Cheng, C.-G. Wang, Z.-P. Guo, P. Zhang, G.-D. Du, H.-K. Liu, *J. Phys. Chem. C* **2009**, *113*, 14518.
- [6] D. Fujimoto, N. Kuwata, Y. Matsuda, J. Kawamura, F. Kang, *Thin Solid Films* **2015**, *579*, 81.
- [7] A. Patil, V. Patil, D.-W. Shin, J.-W. Choi, D.-S. Paik, S.-J. Yoon, *Mater. Res. Bull.* **2008**, *43*, 1913.
- [8] M. N. Obrovac, L. Christensen, *Electrochim. Solid-State Lett.* **2004**, *7*, A93.
- [9] G.-N. Zhu, Y.-G. Wang, Y.-Y. Xia, *Energy Environ. Sci.* **2012**, *5*, 5325.
- [10] Y. Liu, Y. Yang, *J. Nanomater.* **2016**, *2016*, 8123652.
- [11] B. O'Regan, M. Grätzel, *Nature* **1991**, *353*, 737.
- [12] A. K. Haridas, B. Gangaja, P. Srikrishnarka, G. E. Unni, A. S. Nair, S. V. Nair, D. Santhanagopalan, *J. Power Sources* **2017**, *345*, 50.
- [13] A. Lakshmi-Narayana, L. Zhang, C. Jiao, C. M. Julien, Y. Qiu, *Ceram. Int.* **2020**, *46*, 10299.
- [14] M. Curcio, A. De Bonis, S. Brutti, A. Santagata, R. Teghil, *Appl. Surf. Sci. Adv.* **2021**, *4*, 100090.
- [15] M. Létiche, E. Eustache, J. Freixas, A. Demortière, V. De Andrade, L. Morgenroth, P. Tilmant, F. Vaurette, D. Troadec, P. Roussel, T. Brousse, C. Lethien, *Adv. Energy Mater.* **2017**, *7*, 1601402.
- [16] E. Eustache, P. Tilmant, L. Morgenroth, P. Roussel, G. Patriarche, D. Troadec, N. Rolland, T. Brousse, C. Lethien, *Adv. Energy Mater.* **2014**, *4*, 1301612.
- [17] T. Djenizian, I. Hanzu, P. Knauth, *J. Mater. Chem.* **2011**, *21*, 9925.
- [18] T. Ohzuku, T. Kodama, T. Hirai, *J. Power Sources* **1985**, *14*, 153.

- [19] M. Wagemaker, R. Van de Krol, A. P. M. Kentgens, A. A. Van Well, F. M. Mulder, *J. Am. Chem. Soc.* **2001**, *123*, 11454.
- [20] M. Wagemaker, A. P. M. Kentgens, F. M. Mulder, *Nature* **2002**, *418*, 397.
- [21] R. J. Cava, D. W. Murphy, S. Zahurak, A. Santoro, R. S. Roth, *J. Solid State Chem.* **1984**, *53*, 64.
- [22] M. Wagemaker, G. J. Kearley, A. Van Well, H. Mutka, F. M. Mulder, *J. Am. Chem. Soc.* **2003**, *125*, 840.
- [23] R. Baddour-Hadjean, S. Bach, M. B. Smirnov, J. P. Pereira-Ramos, *J. Raman Spectrosc.* **2004**, *35*, 577.
- [24] M. B. Smirnov, R. Baddour-Hadjean, *J. Chem. Phys.* **2004**, *121*, 2348.
- [25] L. J. Hardwick, M. Holzapfel, P. Novák, L. Dupont, E. Baudrin, *Electrochim. Acta* **2007**, *52*, 5357.
- [26] B. Laskova, O. Frank, M. Zukalova, M. Bousa, M. Dracinsky, L. Kavan, *Chem. Mater.* **2013**, *25*, 3710.
- [27] M. Wagemaker, W. J. H. Borghols, F. M. Mulder, *J. Am. Chem. Soc.* **2007**, *129*, 4323.
- [28] K. Shen, H. Chen, F. Klaver, F. M. Mulder, M. Wagemaker, *Chem. Mater.* **2014**, *26*, 1608.
- [29] U. Lafont, D. Carta, G. Mountjoy, A. V. Chadwick, E. M. Kelder, *J. Phys. Chem. C* **2009**, *114*, 1372.
- [30] G. Sudant, E. Baudrin, D. Larcher, J. M. Tarascon, *J. Mater. Chem.* **2005**, *15*, 1263.
- [31] Z. Yang, D. Choi, S. Kerisit, K. M. Rosso, D. Wang, J. Zhang, G. Graff, J. Liu, *J. Power Sources* **2009**, *192*, 588.
- [32] L. Kavan, M. Grätzel, J. Rathousky, A. Zukal, *J. Electrochem. Soc.* **1996**, *143*, 394.
- [33] V. Subramanian, A. Karki, K. I. Gnanasekar, F. P. Eddy, B. Rambabu, *J. Power Sources* **2006**, *159*, 186.
- [34] P. Kubiak, T. Fröschl, N. Hüsing, U. Hörmann, U. Kaiser, R. Schiller, C. K. Weiss, K. Landfester, M. Wohlfahrt-Mehrens, *Small* **2011**, *7*, 1690.
- [35] R. V. De Krol, A. Goossens, E. A. Meulenkamp, *J. Electrochem. Soc.* **1999**, *146*, 3150.
- [36] R. Baddour-Hadjean, J. P. Pereira-Ramos, *Chem. Rev.* **2010**, *110*, 1278.
- [37] R. Baddour-Hadjean, V. Golabkan, J. P. Pereira-Ramos, A. Mantoux, D. Lincot, *J. Raman Spectrosc.* **2002**, *33*, 631.
- [38] R. Baddour-Hadjean, J. P. Pereira-Ramos, C. Navone, M. Smirnov, *Chem. Mater.* **2008**, *20*, 1916.
- [39] A. Bhatia, C. Leviel, M. Hallot, J. P. Pereira-Ramos, C. Lethien, P. Roussel, R. Baddour-Hadjean, *Adv. Mater. Interfaces* **2022**, *9*, 2200733.
- [40] N. N. Dinh, N. T. T. Oanh, P. D. Long, M. C. Bernard, A. H.-L. Goff, *Thin Solid Films* **2003**, *423*, 70.
- [41] B. D. Piercy, C. Z. Leng, M. D. Loego, *J. Vac. Sci. Technol. A* **2017**, *35*, 03E107.
- [42] O. M. E. Ylivaara, A. Langner, X. Liu, D. Schneider, J. Julin, K. Arstila, S. Sintonen, S. Ali, H. Lipsanen, T. Sajavaara, S.-P. Hannula, R. L. Puurunen, *Thin Solid Films* **2021**, *732*, 138758.
- [43] M. Hallot, B. Caja-Munoz, C. Leviel, O. I. Lebedev, R. Retoux, J. Avila, P. Roussel, M. C. Asensio, C. Lethien, *ACS Appl. Mater. Interfaces* **2021**, *13*, 15761.
- [44] a) V. Petricek, M. Dusek, L. Palatinus, *Z. Kristallogr.* **2014**, *229*, 345.
b) A. Coelho, R. W. Cheary, *J. Appl. Cryst.* **1992**, *25*, 109.
- [45] D. Krishnamurti, *Proc. Ind. Acad. Sci. A* **1962**, *55*, 290.
- [46] T. Ohsaka, F. Izumi, Y. Fujiki, *J. Raman Spectrosc.* **1978**, *7*, 321.
- [47] G. A. Tompsett, G. A. Bowmaker, R. P. Cooney, J. B. Metson, K. A. Rodgers, J. M. Seakins, *J. Raman Spectrosc.* **1995**, *26*, 57.
- [48] U. Balachandran, N. G. Eror, *J. Solid State Chem.* **1982**, *42*, 276.
- [49] A. R. Armstrong, G. Armstrong, J. Canales, P. G. Bruce, *Angew. Chem., Int. Ed.* **2004**, *43*, 2286.
- [50] L. Kavan, M. Zukalova, M. Ferus, J. Kürti, J. Koltai, S. Civiš, *Phys. Chem. Chem. Phys.* **2011**, *13*, 11583.
- [51] O. Frank, M. Zukalova, B. Laskova, J. Kürti, J. Koltai, L. Kavan, *Phys. Chem. Chem. Phys.* **2012**, *14*, 14567.
- [52] M. Giarola, A. Sanson, F. Monti, G. Mariotto, M. Bettinelli, A. Speghini, G. Salviulo, *Phys. Rev. B* **2010**, *81*, 174305.
- [53] M. V. Koudriachova, S. W. de Leeuw, N. M. Harrison, *Phys. Rev. B* **2004**, *69*, 054106.